JOURNAL OF SOLID STATE CHEMISTRY 64, 123–133 (1986)

Structural and Magnetic Properties of $MnAs_{0.90}P_{0.10}$

HELMER FJELLVÅG, ARNE KJEKSHUS, AND SVEIN STØLEN

Department of Chemistry, University of Oslo, Blindern, N-0315 Oslo 3, Norway

Received October 22, 1985

$MnAs_{0.90}P_{0.10}$ takes the orthorhombic MnP type structure at temperatures below the second-order transition temperature $T_D = 449 \pm 2$ K, and the hexagonal NiAs type structure between T_D and the melting point $T_m = 1189 \pm 10$ K. The structural changes, in positional parameters and unit cell dimensions (as well as interatomic distances), have been determined for the increasing distortion at temperatures below T_D by means of powder X-ray and neutron diffraction. At low temperatures two distinct incommensurate magnetic structures are found, respectively, over the temperature intervals $0 < T < T_{S1} = 105 \pm 5$ K and $T_{S2} = 185 \pm 5 < T < T_N = 237 \pm 5$ K, whereas a ferromagnetic spin arrangement prevails over the intermediate temperature range $T_{S1} < T < T_{S2}$.

Introduction

Extensive investigations have been carried out on the As-rich side of the $MnAs_{1-x}P_x$ phase using several different experimental techniques [see (*1*) and references therein]. MnAs itself takes the hexagonal NiAs type structure at high [in a paramagnetic (P) state] and low [ferromagnetic (F) state] temperatures, whereas the orthorhombic MnP type structure prevails over a limited temperature range (in a P state). By substituting phosphorous for arsenic in MnAs, the MnP type phase is stabilized, and the NiAs type structure occurs only at elevated temperature (above the transition temperature T_D). This is outlined in the schematic phase diagram shown in Fig. 1. The stabilization of the MnP type structure gives rise to many interesting phenomena, in particular, to intriguing low-temperature magnetic properties.

The first magnetic phase diagram for $MnAs_{1-x}P_x$ was published by Roger and Fruchart (*2*). It was later realized that substitution of phosphorous has a similar effect on the structural and magnetic properties as the application of hydrostatic pressure to (binary) MnAs (*3*, *4*). The recent neutron diffraction study (*1*) for $x = 0.08$ and 0.12 confirmed the existence of low-temperature (magnetic) order–order transitions (cf. the transition lines T_S, T_{S1}, and T_{S2} in Fig. 1). However, some problems remain partly open, inter alia: (i) confirmation of the magnetic state of the intermediate ($T_{S1} < T < T_{S2}$) phase and (ii) clarification of the magnetic structure for $0 < T < T_{S1}$ [cf. (*1*, *5*)]. This work concerns the properties of $MnAs_{0.90}P_{0.10}$ which, as seen from Fig. 1, involves the problems mentioned above.

Also the high-temperature structural and magnetic properties of $MnAs_{1-x}P_x$ are challenging. The second-order MnP ⇄ NiAs type transition takes place not far above room temperature, and offers for $x = 0.10$ a

0022-4596/86 $3.00

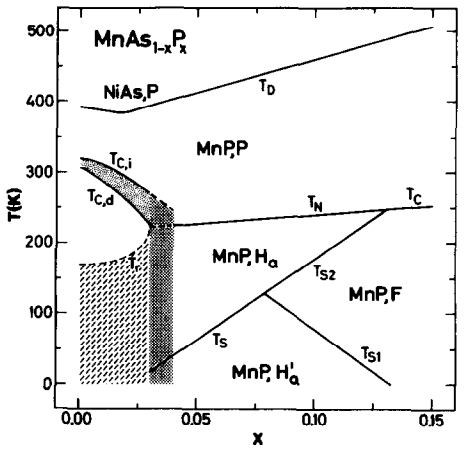

FIG. 1. Schematic phase diagram for $MnAs_{1-x}P_x$, $0.00 \leqq x \leqq 0.15$.

good possibility to study how the unit cell dimensions and the unconstrained positional parameters of the MnP type structure vary upon approaching T_D. The structural data obtained from powder X-ray and neutron diffraction studies of $MnAs_{0.90}P_{0.10}$ are related to the findings for the corresponding state in other, similar phases.

Experimental

The pure elements used as starting materials for the syntheses were 99.99% Mn flakes, 99.9999% P lumps, and 99.9999% As lumps (Koch-Light Laboratories). MnP and MnAs were synthesized by heating stoichiometric quantities of the components in evacuated, sealed silica capsules. The temperature in the horizontally positioned furnaces was slowly increased (3 × 30 K/day) up to 900°C. After cooling to room temperature over 1 day, the samples were carefully crushed and subjected to one further annealing at 900°C for 1 week. The ternary samples of $MnAs_{0.90}P_{0.10}$ were synthesized similarly from MnP and MnAs. After a first heat treatment at 900°C for 5 days the samples were crushed and subjected to a second annealing at 700°C for 4 weeks before being cooled to room temperature over 1 day.

All samples were characterized by room-temperature powder X-ray diffraction [Guinier technique; Cu$K\alpha_1$ radiation; Si as internal standard, a (293 K) = 543.1065 pm (*6*)]. Low- and high-temperature powder X-ray diffraction photographs were obtained between 90 and 1300 K in an Enraf-Nonius (FR 553) Guinier Simon camera (Cu$K\alpha_1$ radiation, quartz crystal monochromatizer). The samples were contained in a rotating, sealed, thin-walled quartz capillary. A Pt-resistance thermometer was used in the temperature regulation, and the difference between the programmed and actual temperature at the sample position is considered to be within ±5 K. The change in temperature was synchronized with the movement of the film casette. The camera factor (including corrections for film shrinkage) for the evaluation of the Guinier Simon photographs was calibrated with the help of the lattice constants obtained for the same sample by the room-temperature Guinier technique. Least-square refinements to obtain unit cell dimensions were performed according to the program CELLKANT (*7*).

Powder neutron diffraction data were recorded between 10 and 293 K with the OPUS III diffractometer accommodated at a radial channel of the JEEP II reactor, Kjeller. Monochromatic neutrons of wavelength 187.7 pm were obtained by reflection from (111) of a Ge crystal. Cylindrical sample holders of vanadium were used. The temperature was controlled and regulated within ±0.5 K by a Thor (3010) controller connected to a Displex cooling system. The Hewat (*8*) version of the Rietveld (*9*) profile refinement program was applied in the final fitting of the crystal structure parameters. Values for the parameters describing the helimagnetic structures (vide infra) were derived from integrated intensities of satellite reflections according to the program SPIRAL (*10*).

Powder neutron diffraction data were also collected on the D1B diffractometer at ILL, Grenoble. The 2θ range 30–110° was covered by a multidetector consisting of 400 cells spaced 0.2° apart, and the neutron wavelength was 251.7 pm. The temperature was continuously increased (10 K/hr) from 300 to 450 K. Accumulated recorded intensities were printed out every 20 min and represent thereby an average over a temperature span of ~3 K. Integrated intensities of Bragg reflections in the diffraction patterns were evaluated by the program INTEGRE (*11*). At temperatures close to T_D, where reflections due to the diminishing orthorhombic distortion ($c/b \approx \sqrt{3}$) overlap, separation of the integrated intensities for overlapping peaks were performed in conformity with LAZY-PULVERIX (*12*) calculations. Positional parameters of the MnP type phase were obtained by least-square refinements of the integrated intensities according to the program SHELX (*13*). Tests were performed in order to check the reliability of the results obtained from data which included integrated intensities separated by the LAZY-PULVERIX evaluation referred to above. When using only well-separated reflections in the refinements, the former results were reproduced within calculated standard deviations. The nuclear scattering lengths, $b_{Mn} = -3.70$, $b_P = 5.1$, and $b_{As} = 6.4$ fm were taken from (*14*). The magnetic formfactor for Mn^{2+} (*15*) was adopted.

Magnetic susceptibilities were measured between 80 and 1000 K by the Faraday method (maximum field ~8 kOe; 10- to 15-mg samples). Differential scanning calorimetry (DSC) measurements were performed with a Mettler TA 3000 system over the temperature range 100–500 K at a heating rate of 10 K/min. Data reduction and evaluation of thermodynamic parameters were performed with standard programs for the system (estimated uncertainty in C_p ± 3%).

Results and Discussion

Structural properties. $MnAs_{0.90}P_{0.10}$ takes the MnP type structure at temperatures $0 < T < T_D = 449 \pm 2$ K [in full agreement with, e.g., (*1*)]. The sharpness of the Bragg reflections and the lack of additional (superstructure) reflections in the powder X-ray and neutron diffraction diagrams, indicate that the P and As atoms are randomly (long range) distributed over the nonmetal sublattice. The structural data for $T \leqq 293$ K fit well with those reported for $x = 0.08$ and 0.12 in (*1*), and agree at 293 K with those of (*2*).

The second-order MnP $\rightleftarrows$ NiAs type transition in $MnAs_{0.90}P_{0.10}$ gives rise to gradual displacements of the Mn and As,P atoms in the orthorhombic MnP type state below T_D (*16–18*). The unit cell dimensions of the two structure types are related by $\mathbf{a}_{MnP} = \mathbf{c}_{NiAs}$, $\mathbf{b}_{MnP} = \mathbf{b}_{NiAs}$, and $\mathbf{c}_{MnP} = 2\mathbf{a}_{NiAs} + \mathbf{b}_{NiAs}$. Increasing orthorhombic distortion is generally reflected in an axial ratio $(c/b)_{MnP}$ which deviates from the ideal orthohexagonal value $\sqrt{3}$ (*17*). The atomic displacement (in terms of space group *Pnma*) within the MnP type unit cell can be represented by $(0, \frac{1}{4}, \frac{1}{4})_{NiAs} \rightarrow (x_{Mn}, \frac{1}{4}, z_{Mn})_{MnP}$ for the metal sublattice and by $(\frac{1}{4}, \frac{1}{4}, \frac{7}{12})_{NiAs} \rightarrow (x_{As,P}, \frac{1}{4}, z_{As,P})_{MnP}$ for the nonmetal sublattice. The direction and magnitude of the displacements $(\frac{1}{4} - z_{Mn}) \approx (\frac{1}{4} - x_{As,P}) \gg x_{Mn} \approx (\frac{7}{12} - z_{As,P})$ are illustrated in Fig. 2. The temperature-induced variations of the parameters x_{Mn} and $(\frac{7}{12} - z_{As,P})$ are rather small, generally within a maximum value of <0.008 at 10 K.

The temperature dependences of $\Delta_{Mn} = \frac{1}{4} - z_{Mn}$ and $\Delta_{As,P} = \frac{1}{4} - x_{As,P}$ for $T \leqq T_D$ are shown in Fig. 3 (for $T > T_D$; $\Delta_{Mn} = \Delta_{As,P} \equiv 0$). The relative changes in these deformation parameters are largest in the temperature range just below T_D, but a smooth variation is found over the entire temperature range. The dotted lines represent the empirical relationship between Δ_T and Δ_X (T and

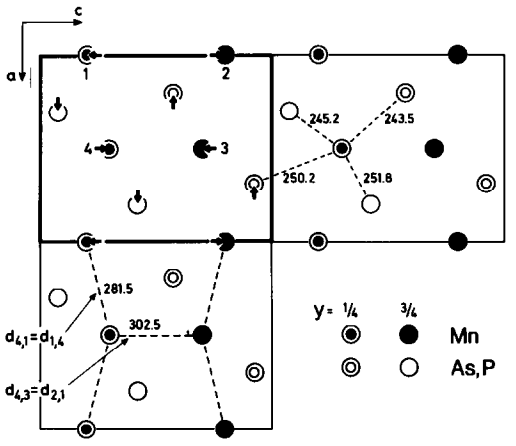

FIG. 2. Projection of the MnP type structure on the *ac* plane. Arrows indicate direction and magnitude of the main atomic displacements from the ideal NiAs type positions. Included are the length (in pm) of the four Mn–As,P bonding distances and the two shortest Mn–Mn distances as well as numbering of Mn atoms. (The third shortest Mn–Mn distance $d_{1,1} = b = 345.3$ pm is parallel to projection axis.)

X denoting metal and nonmetal atoms, respectively) and T/T_D for binary and ternary MnP type phases advanced in (*19*). The latter curves lie below the present Δ_{Mn} and $\Delta_{As,P}$ values for all temperatures below T_D, although tracing out roughly the same temperature dependences. Earlier studies on $Mn_{0.90}Fe_{0.10}As$ (*20*) and $MnAs_{1-x}P_x$ [x = 0.00, 0.08, and 0.20 (*21, 22*)] also report values for the orthorhombic displacements as function of the temperature. The points for $MnAs_{1-x}P_x$ with x = 0.08, 0.12, 0.18, and 0.20 [read from illustrations in (*1, 21, 22*)] are included in Fig. 3 for the purpose of comparison. The results for x = 0.08 and 0.20 lie above (viz. take a larger deformation than) those presently reported. The corresponding values for MnAs and $Mn_{0.90}Fe_{0.10}As$ fit the dotted lines quite well.

The symmetry change at the MnP $\rightleftarrows$ NiAs type transition is as required by the Landau theory for second-order phase transitions (*16*). The results for $MnAs_{0.90}P_{0.10}$ show that in accordance with the direct group–subgroup relationship ($P6_3/mmc$ versus *Pnma*) between the two structure types, the transition proceeds continuously in a diffusionless manner.

The variations of the unit cell dimensions of the MnP and NiAs type states of $MnAs_{0.90}P_{0.10}$ are shown in Fig. 4. At low and high temperatures the thermal expansion [$\alpha_V = (1/V_{293\,K}) \cdot (\partial V/\partial T)$ equals $\sim 9 \times 10^{-5}$ and $\sim 7 \times 10^{-5}$ K^{-1} at 100 and 600 K, respectively] is of "normal" magnitude for MnP type arsenides ($4–10 \times 10^{-5}$ K^{-1}). The thermal expansion of the unit cell edges take maximum values at a temperature somewhat below T_D, with the extraordinary high value $\alpha_V \approx 5 \times 10^{-4}$ K^{-1} at 350 K. At $T \geqq T_D$ the b and $c/\sqrt{3}$ parameters coincide as required by the hexagonal NiAs type symmetry. The progression of the MnP

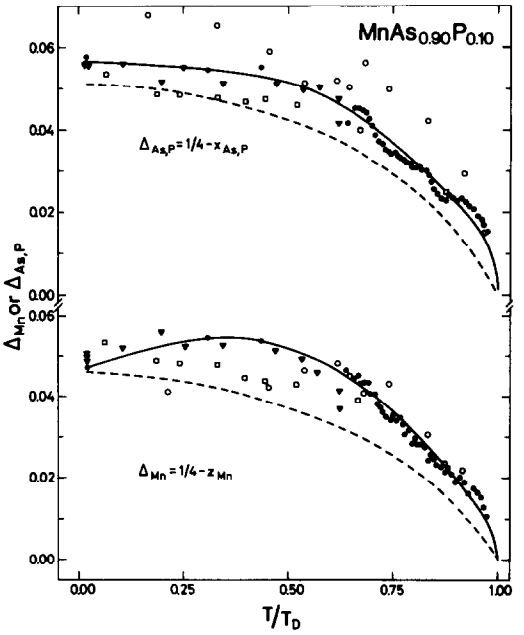

FIG. 3. Variation of the distortion parameters $\Delta_{Mn} = \frac{1}{4} - z_{Mn}$ and $\Delta_{As,P} = \frac{1}{4} - x_{As,P}$ with T/T_D. Dotted curves represent the empirical relationship considered in (*19*), see also text. Present results for x = 0.10 of $MnAs_{1-x}P_x$ are denoted with (●), points marked (▼) are quoted from (*1*) for x = 0.08, 0.12, and 0.18, (□) from (*21*) for x = 0.08, and (○) from (*22*) for x = 0.20.

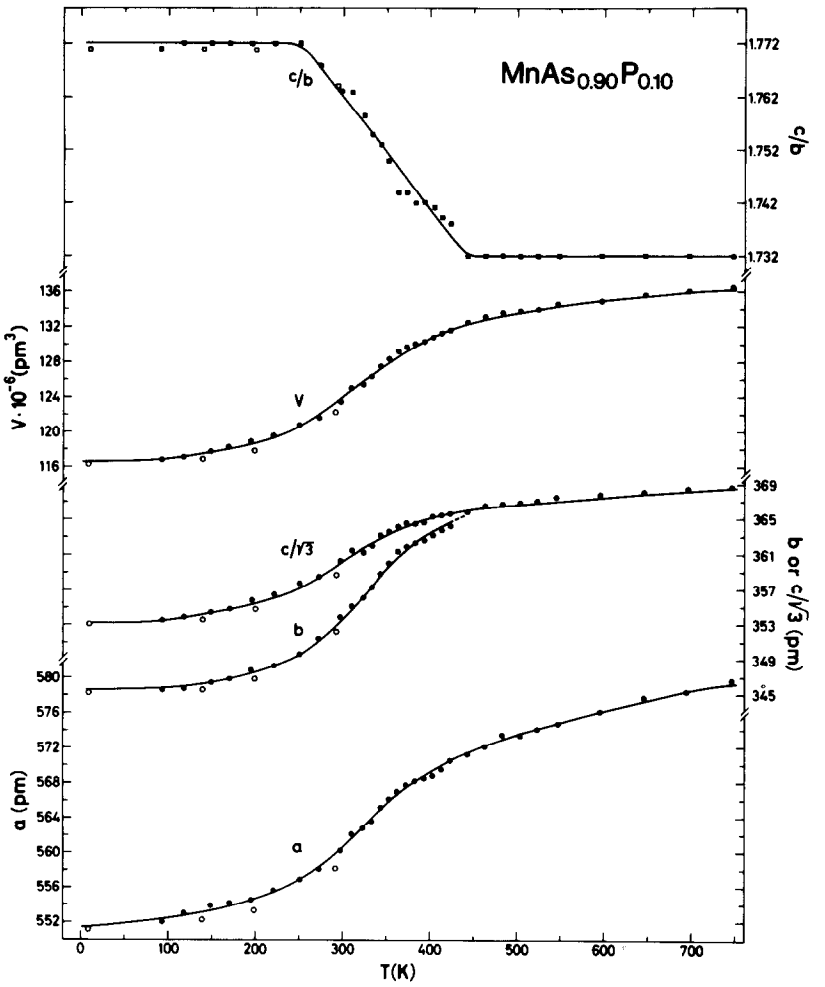

FIG. 4. Temperature dependence of unit cell dimensions for $MnAs_{0.90}P_{0.10}$ between 10 and 750 K. Filled and open symbols represent results obtained by powder X-ray and neutron diffraction, respectively.

type distortion is also evident from the deviation of $\delta = c/b - \sqrt{3}$ from zero. As seen from the upper part of Fig. 4, δ varies approximately linearly with the temperature over the range $250 < T < 450$ K. This concurs well with the findings for $MnAs_{1-x}P_x$ by Suzuki and Ido (*22*). However, in contrast to Δ_T and Δ_X, δ is not useful as a deformation parameter when comparing different MnP type phases which undergo the MnP $\rightleftarrows$ NiAs type transition (*19*). (In several MnP type phases δ deviates only a little from $\sqrt{3}$ whereas Δ_T and Δ_X take large values).

The temperature-induced changes in the crystal structure are illustrated in Fig. 5 which shows the temperature dependences of the two shortest metal–metal distances ($d_{1,4}$ and $d_{2,1}$) and the average metal to nonmetal ($d_{T-X,average}$ for the distorted T–X octahedron) bond length, see Fig. 2. The dotted lines in the inset to Fig. 5 indicate

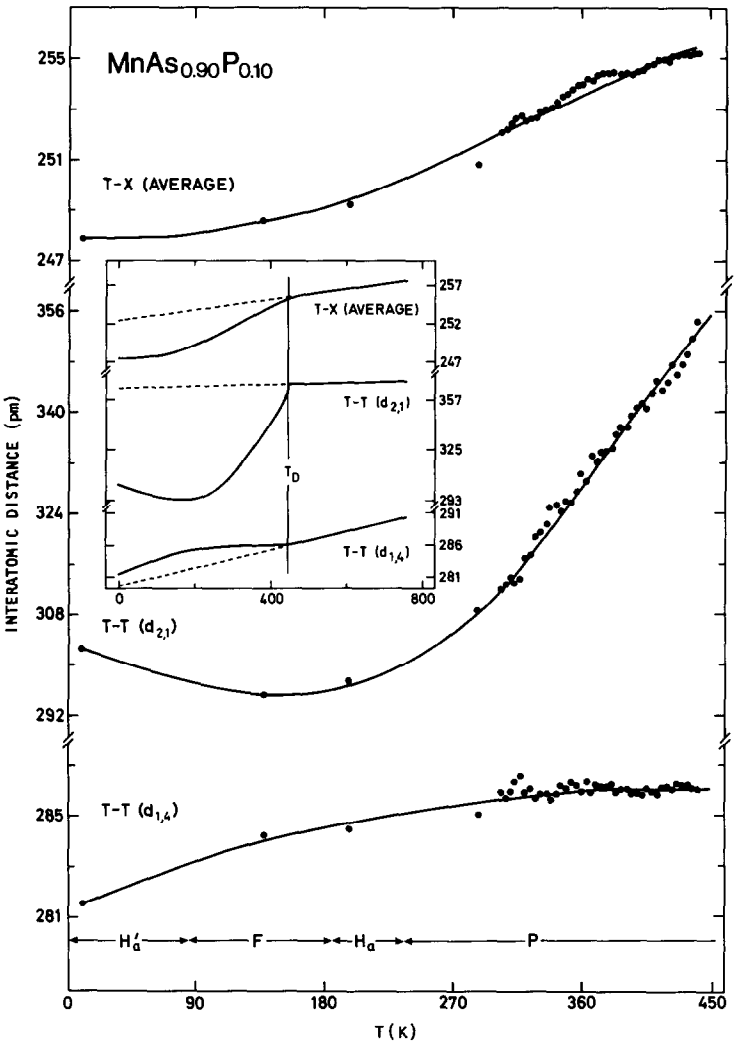

FIG. 5. Variation in selected interatomic distances with temperature between 10 and 800 K. $d_{1,4}$ and $d_{2,1}$ represent shortest and next shortest metal–metal distances while $d_{T-X,average}$ represent the average metal-to-nonmetal bond distance. Magnetic state in MnP type domain is indicated at the bottom. Inset extends the relationships to NiAs,P type state for $T > T_D$.

extrapolated values for the NiAs type state. Upon cooling below T_D, $d_{1,4}$ increases slightly relative to that expected for the NiAs type state, whereas a drastic reduction is found for (in particular) $d_{2,1}$ and $d_{T-X,average}$. The latter distance is 248.0 pm at 10 K compared to 252.4 pm for the extrapolated NiAs type state. This probably reflects that electronic (and in this case also magnetic) features of the Mn atoms are different in the MnP and NiAs type regions. On the other hand, the onset of magnetic long-range order and the magnetic order–order transitions within the MnP type domain are not reflected in (substantial) changes in the crystal structure.

The temperature dependence of the integrated intensity of the MnP type 101 re-

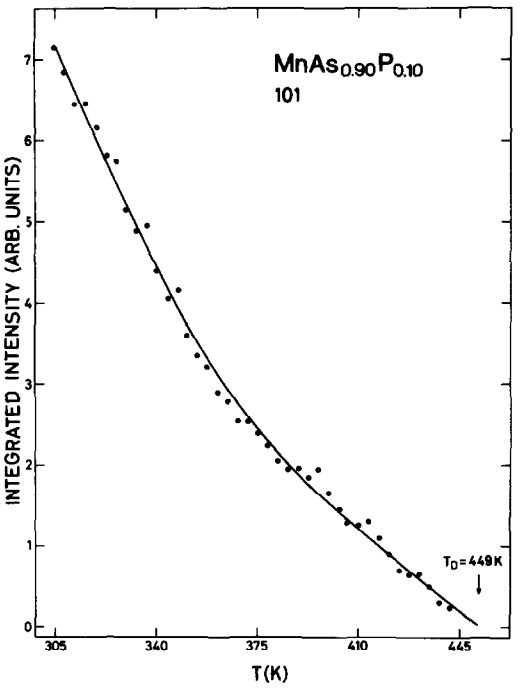

FIG. 6. Variation in integrated intensity of 101 reflection versus temperature as determined by powder neutron diffraction.

flection for temperatures between 300 and T_D is shown in Fig. 6. The smooth variation complies with the results shown in Figs. 3 and 4. The change in slope at ~350 K occurs in close proximity to the temperature of the so-called high–low spin transition [vide infra and (*23–29*)]. Rietveld refinements of powder neutron diffraction data for $T_N < T < T_D$ show that there are definitely no ordered magnetic structure in this temperature interval.

A recent study on $Mn_{1-t}Cr_tAs$ (*30*) has revealed that both the low- and high-temperature properties of this phase are strongly influenced by what is believed to be uncompensated stress in the samples. A phenomenon which may well have the same origin was observed during the syntheses of the $MnAs_{0.90}P_{0.10}$ samples. The room-temperature unit cell dimensions, as derived from Guinier photographic data, were found to increase between subsequent annealings (totally amounting to a 1.3% change in the unit cell volume). The powder X-ray diffraction reflections on each film were sharp and no additional phase(s) could be detected. It is tempting to suggest that the presence of stress fields due to fluctuations in dislocation densities and/or As,P distribution, perhaps coupled to changes in the magnetic state of the Mn atoms, give rise to the observed nonequilibrium properties for $MnAs_{0.90}P_{0.10}$. The structural changes in the transfer stage on the approach to equilibrium were accompanied by variations in the magnetic moment of the high-temperature NiAs type phase as probed by magnetic susceptibility measurements.

Magnetic properties. The phase diagram in Fig. 1 exposes three regions with different magnetic long-range order for the composition $x = 0.10$. The helimagnetic regions for $T_{S2} < T < T_N$ and $0 < T < T_{S1}$ have earlier been established for $x = 0.12$ (*1, 5*). The incommensurate magnetic spiral structures are unequivocally manifested by the presence of satellite reflections in the neutron diffraction patterns. The temperature dependence of $000^{\pm}$ for $MnAs_{0.90}P_{0.10}$ shown in the lower part of Fig. 7 concurs, as will be discussed below, with the phase diagram (Fig. 1). No hysteresis was observed.

All the observed satellite reflections ($hk0^{\pm}$ with $h = 2n + 1$ absent) at 200 K could be indexed as required by the so-called H_a type magnetic structure. A projection of the H_a type structure on the *ac* plane is shown on Fig. 8. The magnetic moments ($\mu_H = 1.45 \pm 0.10\ \mu_B$) are confined to the *bc* plane perpendicular to the propagation vector ($\tau_a/2\pi\mathbf{a}^* = 0.099 \pm 0.001$). A phase difference ($\phi_{1,2} = 51 \pm 8°$) exists between the spirals running through the two sets of Mn atoms ($x, \frac{1}{4}, z; \frac{1}{2} + x, \frac{1}{4}, \frac{1}{2} - z$ and $\bar{x}, \frac{3}{4}, \bar{z}; \frac{1}{2} - x, \frac{3}{4}, \frac{1}{2} + z$, respectively). A

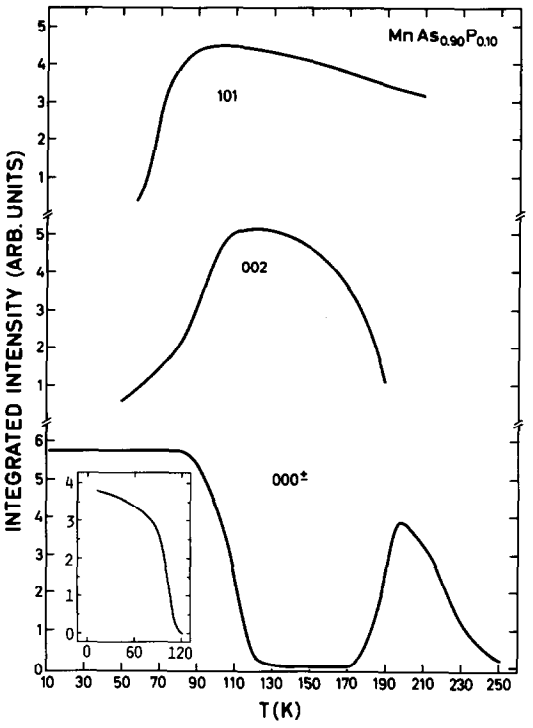

FIG. 7. Temperature dependence of integrated intensity of the magnetic part of the 101 and 002 reflections (see text) and the magnetic 000± satellite for $T < 250$ K. Inset shows corresponding relationship for the extra satellite (see text).

comparison between observed and calculated intensities is given in Table I.

For $0 < T < T_{S1} = 105 \pm 5$ K the satellite reflections could, with one exception, also be indexed according to the H_a type. However, one satellite at $d = 294.8$ pm (10 K) could not be indexed in this way. A corresponding satellite is also present in the low-temperature neutron diffraction diagrams of the samples with $x = 0.08$ and 0.12 (*1*). The temperature dependence of the integrated intensity of this satellite is shown in the inset to Fig. 8, and its intensity vanishes at T_{S1}. Its presence is one of several circumstantial evidences (*5*) for maintaining that the helimagnetic structure (H_a') for $0 < T < T_{S1}$ differs from the H_a type for $T_{S2} < T$

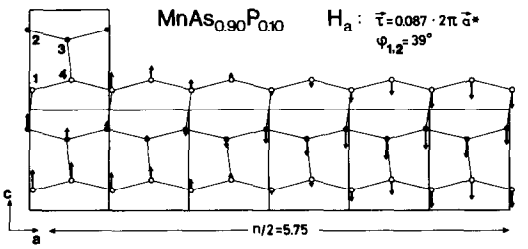

FIG. 8. Projection of the H_a type magnetic structure on *ac* plane. Magnetic moments rotate in *bc* plane.

$< T_N$, cf. Fig. 1. The experimental facilities did not permit verification of a double structure (*5*) in 000± for $x = 0.10$.

The parameters for the H_a' type structure refined in terms of the H_a model are $\tau_a/2\pi\mathbf{a}^* = 0.087 \pm 0.001$, $\phi_{1,2} = 39 \pm 8°$ and $\mu_H = 1.50 \pm 0.10\ \mu_B$ at 10 K. Observed and calculated intensities are listed in Table I, which shows that the fit is much poorer for the 10 K than for the 200 K data. (The Rietveld analysis for the 10 K data gave $R_N = 0.10$, which is about twice the values obtained at $T_{S2} < T < 293$ K. This possibly indicates the presence of additional satellites that are not corrected for, and which overlap with nuclear reflections.) The hint in (*1*) that the extra satellite may reflect coexistence of H_a type helimagnetism and collinear antiferromagnetism seems not to be justified since

TABLE I

OBSERVED AND CALCULATED INTEGRATED INTENSITIES FOR HELIMAGNETIC SATELLITES OF $MnAs_{0.90}P_{0.10}$ AS DERIVED BY REFINEMENTS OF POWDER NEUTRON DIFFRACTION DATA

T(K)	10		200	
hkl	I_{obs}	I_{calc}	I_{obs}	I_{calc}
001±	683	681	964	938
101⁻	651	362	329	353
101⁺	174	279	201	265
200⁻	1036	960	745	745
211⁻	837	904	700	673
211⁺	—	—	454	489

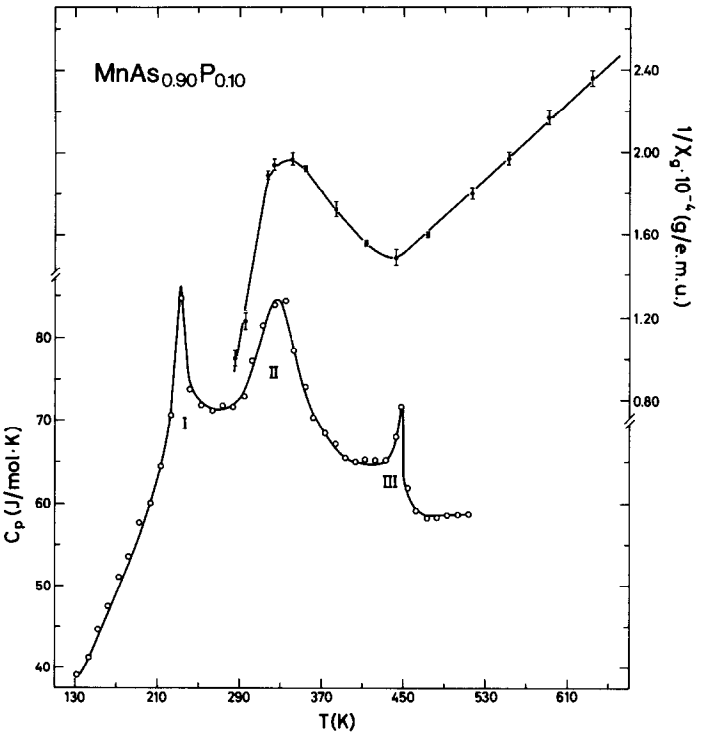

FIG. 9. Heat capacity and inverse magnetic susceptibility of $MnAs_{0.90}P_{0.10}$ for temperatures below 600 K.

the compositional (x) dependence of the d value for the thus implied antiferromagnetic 110 reflection goes in the opposite direction to that observed for the extra satellite. The H_a and H_a' phases are, however, difficult to study by powder diffraction since all satellites are of rather low intensity and often overlap with nuclear reflections. Attempts are therefore made to grow single crystals of $MnAs_{1-x}P_x$ so that the problems associated with the magnetic structures can be solved from single crystal neutron diffraction data. However, we presently firmly believe that H_a and H_a' represent distinct magnetic structures.

A prime goal of the present low-temperature neutron diffraction study was to substantiate the magnetic properties of the intermediate phase for $T_{S1} < T < T_{S2} = 185 \pm 5$ K. In the previous study (*1*) for $x = 0.12$ this phase was believed most probably to be ferromagnetic, although this could not be proved unequivocally from the Rietveld analyses.

The temperature dependences of the magnetic part of the integrated intensities of the 101 and 002 reflections are shown in Fig. 7. The integrated intensities are corrected for changes introduced by temperature variations in the positional parameters of the Mn and As,P atoms. Thus the curves presented should reflect magnetic contributions to these basically nuclear reflections. The pronounced maximum in I_{002} for $T_{S1} < T < T_{S2}$ (and to a lesser degree for I_{101}) strongly supports the inference of a ferromagnetic spin arrangement for the intermediate phase. No clear transitions, at T_{S1} or T_{S2}, are evident from the I_{002} and I_{101} versus temperature relationships. However, al-

though conceivable, no ferromagnetic components could be established by the profile refinements for $0 < T < T_{S1}$ and $T_{S2} < T < T_N$. For the intermediate phase $\mu_F = 1.37 \pm 0.8\ \mu_B$, with magnetic moments parallel to the *b* axis, was obtained at 140 K. (No peak in the heat capacity is detected at T_{S2}.) In order to definitely settle the questions concerning ferromagnetism at low temperatures in $MnAs_{1-x}P_x$ (and its quaternary derivative $Mn_{1-t}Cr_tAs_{1-x}P_x$) a careful examination by polarized neutrons will be undertaken.

For the temperatures above $T_N = 237 \pm 5$ K paramagnetism prevails, in the domains of both the MnP and NiAs type structures, cf. Fig. 1. However, the rather large change in the structural arrangement between T_N and T_D (vide supra) is accompanied by anomalous paramagnetic behaviour [cf., e.g., (*23–25, 31*)]. For $T > T_D$ the magnetic susceptibility can be described according to the Curie–Weiss law ($\theta = 130 \pm 18$ K, μ_{eff} $4.63 \pm 0.04\ \mu_B$ giving $2S = 3.74 \pm 0.04$ according to the spin only approximation $\mu_{eff} = g\sqrt{S(S+1)}$ with $g = 2$). The number of unpaired electrons is accordingly reduced from ~3.7 for $T > T_D$ to ~1.5 at 10 K (which is appreciable even when the difference in methodology is considered), and a so-called high- to low-spin transition in the MnP,P type region is advanced as an explanation (*23–29*).

The results of DSC measurements are shown in Fig. 9. The low-temperature peak I reflects the spin ordering at T_N and the high-temperature peak III the MnP ⇄ NiAs type transition. The intermediate anomaly (II) has been ascribed to the paramagnetic high- to low-spin transition, and our experimental findings thus confirm those of (*28*). The DSC anomaly II correlates with the region of anomalous paramagnetism (Fig. 9) and the range of enhanced thermal expansion. However, this complex phenomenon is presently further explored by NMR and neutron diffraction diffuse scattering measurements, and a discussion of the change in the properties within the domain of the MnP,P type phase is conveniently postponed.

Acknowledgment

The authors are grateful to Institut Max von Laue–Paul Langevin, Grenoble, for providing facilities for neutron diffraction measurements.

References

1. H. FJELLVÅG, A. F. ANDRESEN, AND K. BÄRNER, *J. Magn. Magn. Mater.* **46,** 29 (1984).
2. A. ROGER AND R. FRUCHART, *Mater. Res. Bull.* **3,** 253 (1968).
3. S. HANEDA, N. KAZAMA, Y. YAMAGUCHI, AND H. WATANABE, *J. Phys. Soc. Japan* **42,** 1212 (1977).
4. N. MENYUK, J. A. KAFALAS, K. DWIGHT, AND J. B. GOODENOUGH, *Phys. Rev.* **177,** 942 (1969).
5. H. FJELLVÅG, A. KJEKSHUS, AND A. F. ANDRESEN, *J. Magn. Magn. Mater.* **50,** 287 (1985).
6. R. D. DESLATTERS AND A. HENINS, *Phys. Rev. Lett.* **31,** 972 (1973).
7. N. O. ERSSON, private communication.
8. A. W. HEWAT, "The Rietveld Computer Program for the Profile Refinement of Neutron Diffraction Powder Patterns Modified for Anisotropic Thermal Vibrations," UKAERE Harwell Report RRL 73/897 (1973).
9. H. M. RIETVELD, *J. Appl. Crystallogr.* **2,** 65 (1969).
10. J. E. ENGEBRETSEN, "Computer Programmes for Elastic Scattering of Neutrons from Crystalline Powders," IFA, Kjeller (1970).
11. P. WOLFERS, "Programs for Treatment of Powder Profiles," ILL, Grenoble (1975).
12. K. YVON, W. JEITSCHKO, AND E. PARTHÉ, *J. Appl. Crystallogr.* **10,** 73 (1977).
13. C. SHELDRICK, "SHELX—Programme for Crystal Structure Determination" (1976).
14. G. E. BACON, *in* (W. B. Yelon, Ed.) *Neutron Diffraction Newsletter* (1977).
15. R. E. WATSON AND A. J. FREEMAN, *Acta Crystallogr.* **14,** 27 (1961).
16. H. F. FRANZEN, C. HAAS, AND F. JELLINEK, *Phys. Rev. B* **10,** 1248 (1974).
17. K. SELTE AND A. KJEKSHUS, *Acta Chem. Scand.* **27,** 3195 (1973).
18. K. ENDRESEN, S. FURUSETH, K. SELTE, A. KJEKSHUS, T. RAKKE, AND A. F. ANDRESEN, *Acta Chem. Scand. A* **31,** 249 (1977).

19. H. FJELLVÅG AND A. KJEKSHUS, *J. Solid State Chem.* **59,** 9 (1985).
20. K. SELTE, A. KJEKSHUS, AND A. F. ANDRESEN, *Acta Chem. Scand.* **27,** 3607 (1973).
21. E. L. HALL, L. H. SCHWARTZ, G. P. FELCHER, AND D. H. RIDGLEY, *J. Appl. Phys.* **41,** 939 (1970).
22. T. SUZUKI AND H. IDO, *J. Phys. Soc. Japan* **51,** 3149 (1982).
23. J. B. GOODENOUGH, D. H. RIDGLEY, AND W. A. NEWMAN, in "Proceedings, International Conference on Magnetism," p. 542, Nottingham (1964).
24. H. IDO, *J. Phys. Soc. Japan* **25,** 1543 (1968).
25. L. H. SCHWARTZ, E. L. HALL, AND G. P. FELCHER, *J. Appl. Phys.* **42,** 1621 (1971).
26. S. HANEDA, N. KAZAMA, Y. YAMAGUCHI, AND H. WATANABE, *J. Phys. Soc. Japan* **42,** 31 (1977).
27. S. HANEDA, Y. YAMAGUCHI, H. WATANABE, AND N. KAZAMA, *J. Phys. Soc. Japan* **46,** 802 (1979).
28. H. J. KROKOSZINSKI, C. SANTANDREA, E. GMELIN, AND K. BÄRNER, *Phys. Status Solidi B* **113,** 185 (1982).
29. K. MOTIZUKI AND K. KATOH, *J. Phys. Soc. Japan* **53,** 735 (1984).
30. A. F. ANDRESEN, K. BÄRNER, H. FJELLVÅG, K. HEINEMANN, A. KJEKSHUS, AND U. SONDERMANN, *J. Magn. Magn. Mater.* **58,** 287 (1986).
31. R. WÖHL AND K. BÄRNER, *J. Magn. Magn. Mater.* **21,** 80 (1980).